28. Dark Energy

Revised August 2023 by D.H. Weinberg (Ohio State U.) and M. White (UC Berkeley; LBNL).

28.1 Repulsive Gravity and Cosmic Acceleration

In the first modern cosmological model, Einstein [1] modified his field equation of General Relativity (GR), introducing a "cosmological term" that enabled a solution with time-independent, spatially homogeneous matter density $\rho_{\rm m}$ and constant positive space curvature. Although Einstein did not frame it this way, one can view the "cosmological constant" Λ as representing a constant energy density of the vacuum [2], whose repulsive gravitational effect balances the attractive gravity of matter and thereby allows a static solution. After the development of dynamic cosmological models [3,4] and the discovery of cosmic expansion [5], the cosmological term appeared unnecessary, and Einstein and de Sitter [6] advocated adopting an expanding, homogeneous and isotropic, spatially flat, matter-dominated Universe as the default cosmology until observations dictated otherwise. Such a model has matter density equal to the critical density, $\Omega_{\rm m} \equiv \rho_{\rm m}/\rho_{\rm c} = 1$, and negligible contribution from other energy components [7].

By the mid-1990s, the Einstein-de Sitter model was showing numerous cracks, under the combined onslaught of data from the cosmic microwave background (CMB), large-scale galaxy clustering, and estimates of the matter density, the expansion rate (H_0), and the age of the Universe. As noted in a number of papers from this time, introducing a cosmological constant offered a potential resolution of many of these tensions, yielding the most empirically successful version of the inflationary cold dark matter scenario. In the late 1990s, supernova surveys by two independent teams provided direct evidence for accelerating cosmic expansion [8,9], establishing the cosmological constant model (with $\Omega_{\rm m} \simeq 0.3$, $\Omega_\Lambda \simeq 0.7$) as the preferred alternative to the $\Omega_{\rm m} = 1$ scenario. Shortly thereafter, CMB evidence for a spatially flat Universe [10,11], and thus for $\Omega_{\rm tot} \simeq 1$, cemented the case for cosmic acceleration by firmly eliminating the free-expansion alternative with $\Omega_{\rm m} \ll 1$ and $\Omega_\Lambda = 0$. Today, the accelerating Universe is well established by multiple lines of independent evidence from a tight web of precise cosmological measurements.

As discussed in the Big Bang Cosmology article of this *Review* (Sec. 22), the scale factor $R(t)$ of a homogeneous and isotropic Universe governed by GR grows at an accelerating rate if the pressure $p < -\frac{1}{3}\rho$ (in $c = 1$ units). A cosmological constant has $\rho_\Lambda =$ constant and pressure $p_\Lambda = -\rho_\Lambda$ (see Eq. 22.10), so it will drive acceleration if it dominates the total energy density. However, acceleration could arise from a more general form of "dark energy" that has negative pressure, typically specified in terms of the equation-of-state-parameter $w = p/\rho$ ($= -1$ for a cosmological constant). Furthermore, the conclusion that acceleration requires a new energy component beyond matter and radiation relies on the assumption that GR is the correct description of gravity on cosmological scales. The title of this article follows the common but inexact usage of "dark energy" as a catch-all term for the origin of cosmic acceleration, regardless of whether it arises from a new form of energy or a modification of GR. Our account here draws on the much longer review of cosmic acceleration in Ref. [12], which provides background explanation and extensive literature references for the discussion in Secs. 28.2 and 28.3.

Below we will use the abbreviation ΛCDM to refer to a model with cold dark matter, a cosmological constant, inflationary initial conditions, standard radiation and neutrino content, and a flat Universe with $\Omega_{\rm tot} = 1$ (though we will sometimes describe this model as "flat ΛCDM" to emphasize this last restriction). We will use wCDM to denote a model with the same assumptions but a free, constant value of w. Models with the prefix "o" (*e.g.*, `owCDM`) allow non-zero space curvature.

28.2 Theories of Cosmic Acceleration

28.2.1 *Dark Energy or Modified Gravity?*

A cosmological constant is the mathematically simplest, and perhaps the physically simplest, theoretical explanation for the accelerating Universe. The problem is explaining its unnaturally small magnitude, as discussed in Sec. 22.4.7 of this *Review*. An alternative (which still requires finding a way to make the cosmological constant zero or at least negligibly small) is that the accelerating cosmic expansion is driven by a new form of energy such as a scalar field [13] with potential $V(\phi)$. The energy density and pressure of the field $\phi(\mathbf{x})$ take the same forms as for inflationary scalar fields, given in Eq. (22.52) of the Big Bang Cosmology article. In the limit that $\frac{1}{2}\dot{\phi}^2 \ll |V(\phi)|$, the scalar field acts like a cosmological constant, with $p_\phi \simeq -\rho_\phi$. In this scenario, today's cosmic acceleration is closely akin to the epoch of inflation, but with radically different energy and timescale.

More generally, the value of $w = p_\phi/\rho_\phi$ in scalar field models evolves with time in a way that depends on $V(\phi)$ and on the initial conditions $(\phi_i, \dot{\phi}_i)$; some forms of $V(\phi)$ have attractor solutions in which the late-time behavior is insensitive to initial values. Many forms of time evolution are possible, including ones where w is approximately constant and broad classes where w "freezes" towards or "thaws" away from $w = -1$, with the transition occurring when the field comes to dominate the total energy budget. If ρ_ϕ is even approximately constant, then it becomes dynamically insignificant at high redshift, because the matter density scales as $\rho_{\rm m} \propto (1+z)^3$. "Early dark energy" models are ones in which ρ_ϕ is a small but not negligible fraction (*e.g.*, a few percent) of the total energy throughout the matter- and radiation-dominated eras, tracking the dominant component before itself coming to dominate at low redshift.

Instead of introducing a new energy component, one can attempt to modify gravity in a way that leads to accelerated expansion [14]. One option is to replace the Ricci scalar $\mathcal{R}$ with a function $\mathcal{R} + f(\mathcal{R})$ in the gravitational action [15]. Other changes can be more radical, such as introducing extra dimensions and allowing gravitons to "leak" off the brane that represents the observable Universe (the "DGP" model [16]). The DGP example has inspired a more general class of "galileon" and massive gravity models. Constructing viable modified gravity models is challenging, in part because it is easy to introduce theoretical inconsistencies (such as "ghost" fields with negative kinetic energy), but above all because GR is a theory with many high-precision empirical successes on solar system scales [17]. Modified gravity models typically invoke screening mechanisms that force model predictions to approach those of GR in regions of high density or strong gravitational potential. Screening offers potentially distinctive signatures, as the strength of gravity (*i.e.*, the effective value of $G_{\rm N}$) can vary by order unity in environments with different gravitational potentials.

More generally, one can search for signatures of modified gravity by comparing the history of cosmic structure growth to the history of cosmic expansion. Within GR, these two are linked by a consistency relation, as described below (Eq. (28.2)). Modifying gravity can change the predicted rate of structure growth, and it can make the growth rate dependent on scale or environment. In some circumstances, modifying gravity alters the combinations of potentials responsible for gravitational lensing and the dynamics of non-relativistic tracers (such as galaxies or stars) in different ways (see Sec. 22.4.7 in this *Review*), leading to order unity mismatches between the masses of objects inferred from lensing and those inferred from dynamics in unscreened environments.

At present there are no fully realized and empirically viable modified gravity theories that explain the observed level of cosmic acceleration. The constraints on $f(\mathcal{R})$ models now force them so close to GR that they cannot produce acceleration without introducing a separate dark energy component [18]. The DGP model is empirically ruled out by several tests, including the expansion history, the integrated Sachs-Wolfe effect, and redshift-space distortion measurements of the struc-

ture growth rate [19]. The near-simultaneous arrival of gravitational waves and electromagnetic signals from the neutron star merger event GW170817, which shows that gravitational waves travel at almost exactly the speed of light, is a further strong constraint on modified gravity theories [20]. The elimination of models should be considered an important success of the program to empirically test theories of cosmic acceleration. However, it is worth recalling that there was no fully realized gravitational explanation for the precession of Mercury's orbit prior to the completion of GR in 1915, and the fact that no complete and viable modified gravity theory exists today does not mean that one will not arise in the future. In the meantime, we can continue empirical investigations that can tighten restrictions on such theories or perhaps point towards the gravitational sector as the origin of accelerating expansion.

28.2.2 *Expansion History and Growth of Structure*

The main line of empirical attack on dark energy is to measure the history of cosmic expansion and the history of matter clustering with the greatest achievable precision over a wide range of redshift. Within GR, the expansion rate $H(z)$ is governed by the Friedmann equation (see the articles on Big Bang Cosmology and Cosmological Parameters—Secs. 22 and 25 in this *Review*). For dark energy with an equation of state $w(z)$, the cosmological constant contribution to the expansion, Ω_Λ, is replaced by a redshift-dependent contribution. The evolution of the dark energy density follows from Eq. (22.10),

$$\Omega_{\rm de}\frac{\rho_{\rm de}(z)}{\rho_{\rm de}(z=0)} = \Omega_{\rm de}\exp\left[3\int_0^z [1+w(z')]\frac{dz'}{1+z'}\right] \;=\; \Omega_{\rm de}(1+z)^{3(1+w)}, \tag{28.1}$$

where the second equality holds for constant w. If $\Omega_{\rm m}$, $\Omega_{\rm r}$, and the present value of $\Omega_{\rm tot}$ are known, then measuring $H(z)$ pins down $w(z)$. (Note that $\Omega_{\rm de}$ is the same quantity denoted $\Omega_{\rm v}$ in Sec. 22, but we have adopted the 'de' subscript to avoid implying that dark energy is necessarily a vacuum effect.)

While some observations can probe $H(z)$ directly, others measure the distance-redshift relation. The basic relations between angular diameter distance or luminosity distance and $H(z)$ are given in Ch. 22 —and these are generally unaltered in time-dependent dark energy or modified gravity models. For convenience, in later sections, we will sometimes refer to the comoving angular diameter distance, $D_{\rm A,c}(z) = (1+z)D_{\rm A}(z)$.

In GR-based linear perturbation theory, the density contrast $\delta(\mathbf{x},t) \equiv \rho(\mathbf{x},t)/\bar{\rho}(t) - 1$ of pressureless matter grows in proportion to the linear growth function $G(t)$ (not to be confused with the gravitational constant $G_{\rm N}$), which follows the differential equation

$$\ddot{G} + 2H(z)\dot{G} - \frac{3}{2}\Omega_{\rm m}H_0^2(1+z)^3 G = 0\ . \tag{28.2}$$

To a good approximation, the logarithmic derivative of $G(z)$ is

$$f(z) \equiv -\frac{d\ln G}{d\ln(1+z)} \simeq \left[\Omega_{\rm m}(1+z)^3\frac{H_0^2}{H^2(z)}\right]^\gamma\ , \tag{28.3}$$

where $\gamma \simeq 0.55$ for relevant values of cosmological parameters [21]. In an $\Omega_{\rm m} = 1$ Universe, $G(z) \propto (1+z)^{-1}$, but growth slows when $\Omega_{\rm m}$ drops significantly below unity. One can integrate Eq. (28.3) to get an approximate integral relation between $G(z)$ and $H(z)$, but the full (numerical) solution to Eq. (28.2) should be used for precision calculations. Even in the non-linear regime, the amplitude of clustering is determined mainly by $G(z)$, so observations of non-linear structure can be used to infer the linear $G(z)$, provided one has good theoretical modeling to relate the two.

In modified gravity models the growth rate of gravitational clustering may differ from the GR prediction. A general strategy to test modified gravity, therefore, is to measure both the expansion history and the growth history to see whether they yield consistent results for $H(z)$ or $w(z)$.

28.2.3 *Parameters*

Constraining a general history of $w(z)$ is nearly impossible, because the dark energy density, which affects $H(z)$, is given by an integral over $w(z)$, and distances and the growth factor involve a further integration over functions of $H(z)$. Oscillations in $w(z)$ over a range $\Delta z/(1+z) \ll 1$ are therefore extremely difficult to constrain. It has become conventional to phrase constraints or projected constraints on $w(z)$ in terms of a linear evolution model,

$$w(a) = w_0 + w_a(1-a) = w_p + w_a(a_p - a), \tag{28.4}$$

where $a \equiv (1+z)^{-1}$, w_0 is the value of w at $z = 0$, and w_p is the value of w at a "pivot" redshift $z_p \equiv a_p^{-1} - 1$, where it is best constrained by a given set of experiments. For typical data combinations, $z_p \simeq 0.5$. This simple parameterization can provide a good approximation to the predictions of many physically motivated models for observables measured with percent-level precision. A widely used "Figure of Merit" (FoM) for dark energy experiments [22] is the projected combination of errors $[\sigma(w_p)\sigma(w_a)]^{-1}$. Ambitious future experiments with 0.1–0.3% precision on observables can constrain richer descriptions of $w(z)$, which can be characterized by principal components.

There has been less convergence on a standard parameterization for describing modified gravity theories. Deviations from the GR-predicted growth rate can be described by a deviation $\Delta\gamma$ in the index of Eq. (28.3), together with an overall multiplicative offset relative to the $G(z)$ expected from extrapolating the CMB-measured fluctuation amplitude to low redshift. However, these two parameters may not accurately capture the growth predictions of all physically interesting models. Another important parameter to constrain is the ratio of the gravitational potentials governing space curvature and the acceleration of non-relativistic test particles. The possible phenomenology of modified gravity models is rich [23], which enables many consistency tests but complicates the task of constructing parameterized descriptions.

The more general set of cosmological parameters is discussed elsewhere in this *Review* (Sec. 25), but here we highlight a few that are particularly important to the dark energy discussion.

- The dimensionless Hubble parameter $h \equiv H_0/100\ \mathrm{km\,s^{-1}\,Mpc^{-1}}$ determines the present day value of the critical density and the overall scaling of distances inferred from redshifts.
- Ω_m and Ω_{tot} affect the expansion history and the distance-redshift relation.
- The sound horizon $r_s = \int_0^{t_{rec}} c_s(t)dt/a(t)$, the comoving distance that pressure waves can propagate between $t = 0$ and recombination, determines the physical scale of the acoustic peaks in the CMB and the baryon acoustic oscillation (BAO) feature in low-redshift matter clustering [24].
- The amplitude of matter fluctuations, conventionally represented by the quantity $\sigma_8(z)$, scales the overall amplitude of growth measures such as weak lensing or redshift-space distortions (discussed in the next section).

Specifically, $\sigma_8(z)$ refers to the rms fluctuation of the matter overdensity $\rho/\bar{\rho}$ in spheres of radius $8\,h^{-1}$Mpc, computed from the linear theory matter power spectrum at redshift z, and σ_8 on its own refers to the value at $z = 0$ (just like our convention for Ω_m).

While discussions of dark energy are frequently phrased in terms of values and errors on quantities like w_p, w_a, $\Delta\gamma$, and Ω_{tot}, parameter precision is the means to an end, not an end in itself. The

underlying goal of empirical studies of cosmic acceleration is to address two physically profound questions:

- 1. Does acceleration arise from a breakdown of GR on cosmological scales or from a new energy component that exerts repulsive gravity within GR?
- 2. If acceleration is caused by a new energy component, is its energy density constant in space and time, as expected for a fundamental vacuum energy, or does it show variations that indicate a dynamical field?

Substantial progress towards answering these questions, in particular any definitive rejection of the cosmological constant "null hypothesis," would be a major breakthrough in cosmology and fundamental physics.

28.3 Observational Probes

We briefly summarize the observational probes that play the greatest role in current constraints on dark energy. Further discussion can be found in other articles of this *Review*, in particular Secs. 25 (Cosmological Parameters) and 29 (The Cosmic Microwave Background), and in Ref. [12], which provides extensive references to background literature. Recent observational results from these methods are discussed in Sec. 28.4.

28.3.1 *Methods, Sensitivity, Systematics*

Cosmic Microwave Background Anisotropies: Although CMB anisotropies provide limited information about dark energy on their own, CMB constraints on the geometry, matter content, and radiation content of the Universe play a critical role in dark energy studies when combined with low-redshift probes. In particular, CMB data supply measurements of $\theta_{\rm s} = r_{\rm s}/D_{\rm A,c}(z_{\rm rec})$, the angular size of the sound horizon at recombination, from the angular location of the acoustic peaks, measurements of $\Omega_{\rm m}h^2$ and $\Omega_{\rm b}h^2$ from the heights of the peaks, and normalization of the amplitude of matter fluctuations at $z_{\rm rec}$ from the amplitude of the CMB fluctuations themselves. The comoparison of the acoustic scale to the diffusion damping scale helps to constrain the expansion rate near recombination. *Planck* data yield a 0.18% determination of $r_{\rm s}$, which scales as $(\Omega_{\rm m}h^2)^{-0.25}$ for cosmologies with standard matter and radiation content. The uncertainty in the matter fluctuation amplitude at the epoch of recombination is 0.5%. Secondary anisotropies, including the integrated Sachs-Wolfe effect, the Sunyaev-Zeldovich (SZ, [25]) effect, and weak lensing of primary anisostropies, provide additional information about dark energy by constraining low-redshift structure growth.

Type Ia Supernovae (SN): Type Ia supernovae, produced by the thermonuclear explosions of white dwarfs, exhibit 10–15% scatter in peak luminosity after correction for light curve duration (the time to rise and fall) and color (which is a diagnostic of dust extinction). Since the peak luminosity is not known *a priori*, supernova surveys constrain ratios of luminosity distances $D_{\rm L}(z)$ at different redshifts. If one is comparing a high-redshift sample to a local calibrator sample measured with much higher precision (and distances inferred from Hubble's law), then one essentially measures the luminosity distance in h^{-1}Mpc, constraining the combination $hD_{\rm L}(z)$. With distance uncertainties of 5–8% per well observed supernova, a sample of around 100 SNe is sufficient to achieve sub-percent statistical precision. The percent-level systematic uncertainties in current samples are dominated by uncertainties associated with photometric calibration and dust extinction corrections and modeling the correlations among supernova luminosity, color, light-curve shape, and host galaxy properties. Another potential systematic is redshift evolution of the supernova population itself, which can be tested by analyzing subsamples grouped by spectral properties or host galaxy properties to confirm that they yield consistent results. Recent analyses of large supernova compilations calibrate these systematic uncertainties internally in parallel with cosmological constraints, with an overall error

budget that has similar contributions from systematic and statistical uncertainties (e.g., [26]).

Baryon Acoustic Oscillations (BAO): Pressure waves that propagate in the pre-recombination photon-baryon fluid imprint a characteristic scale in the clustering of matter and galaxies, which appears in the galaxy correlation function as a localized peak at the sound horizon scale $r_{\rm s}$, or in the power spectrum as a series of oscillations. Since observed galaxy coordinates consist of angles and redshifts, measuring this "standard ruler" scale in a galaxy redshift survey determines the angular diameter distance $D_{\rm A}(z)$ and the expansion rate $H(z)$, which convert coordinate separations to comoving distances. Errors on the two quantities are correlated, and in existing galaxy surveys the best determined combination is approximately $D_{\rm V}(z) = [czD_{\rm A,c}^2(z)/H(z)]^{1/3}$. As a useful rule of thumb, a survey that fully samples structures at redshift z over a comoving volume V, and is therefore limited by cosmic variance rather than shot noise, measures $D_{\rm A,c}(z)$ with a fractional error of $0.005(V/10\,{\rm Gpc}^3)^{-1/2}$ and $H(z)$ with a fractional error 1.6–1.8 times higher. The most precise BAO measurements to date come from large galaxy redshift surveys probing $z < 0.8$, and these will be extended to higher redshifts by ongoing and future projects. At redshifts $z > 2$, BAO can also be measured in the Lyman-α forest of intergalactic hydrogen absorption towards background quasars, where the fluctuating absorption pattern provides tens or hundreds of samples of the density field along each quasar sightline. For Lyman-α forest BAO, the best measured parameter combination is more heavily weighted towards $H(z)$ because of strong redshift-space distortions that enhance clustering in the line-of-sight direction. Radio intensity mapping, which maps large-scale structure in redshifted 21-cm hydrogen emission without resolving individual galaxies, offers a potential route to measuring BAO over large volumes at relatively low cost, but the technique is still under development. Photometric redshifts in optical imaging surveys can be used to measure BAO in the angular direction, though the typical distance precision is a factor of 3–4 lower compared to a well sampled spectroscopic survey of the same area, and angular BAO measurements do not directly constrain $H(z)$. BAO distance measurements complement SN distance measurements by providing absolute rather than relative distances (with precise calibration of $r_{\rm s}$ from the CMB) and by having greater achievable precision at high redshift thanks to the increasing comoving volume available. Theoretical modeling suggests that BAO measurements from even the largest feasible redshift surveys will be limited by statistical rather than systematic uncertainties.

Weak Gravitational Lensing: Gravitational light bending by a clustered distribution of matter shears the shapes of higher redshift background galaxies in a spatially coherent manner, producing a correlated pattern of apparent ellipticities. By studying the weak lensing signal for source galaxies binned by photometric redshift (estimated from broad-band colors), one can probe the history of structure growth. "Cosmic shear" weak lensing uses the correlation of source ellipticities to deduce the clustering of intervening matter. "Galaxy-galaxy lensing" (GGL) uses the correlation between a shear map and a foreground galaxy sample to measure the average mass profile around the foreground galaxies, which can be combined with galaxy clustering to constrain total matter clustering. For a specified expansion history, the predicted signals scale approximately as $\sigma_8\Omega_{\rm m}^{\alpha}$, with $\alpha \simeq 0.3$–0.5. The predicted signals also depend on the distance-redshift relation, so weak lensing becomes more powerful in concert with SN or BAO measurements that can pin this relation down independently. The most challenging systematics are shape measurement biases, biases in the distribution of photometric redshifts, and intrinsic alignments of galaxy orientations that could contaminate the lensing-induced signal. Weak lensing of CMB anisotropies is an increasingly powerful tool, in part because it circumvents many of these observational and astrophysical systematics. Predicting the large-scale weak lensing signal is straightforward in principle, but the number of independent modes on large scales is small, and the inferences are therefore dominated by sample variance. Exploiting small-scale measurements, for tighter constraints, requires modeling the effects of complex physical processes such as star formation and feedback on the matter power spectrum. Strong gravitational

lensing can also provide constraints on dark energy, either through time delay measurements that probe the absolute distance scale, or through measurements of multiple-redshift lenses that constrain distance ratios. The primary uncertainty for strong lensing constraints is modeling the mass distribution of the lens systems.

Clusters of Galaxies: Like weak lensing, the abundance of massive dark-matter halos probes structure growth by constraining $\sigma_8\Omega_{\rm m}^{\alpha}$, where $\alpha \simeq 0.3$–0.5. These halos can be identified as dense concentrations of galaxies or through the signatures of hot (10^7–$10^8\,$K) gas in X-ray emission or SZ distortion of the CMB. The critical challenge in cluster cosmology is calibrating the relation $P(M_{\rm halo}|O)$ between the halo mass as predicted from theory and the observable O used for cluster identification. Measuring the stacked weak lensing signal from clusters has emerged as a promising approach to achieve percent-level accuracy in calibration of the mean relation, which is required for clusters to remain competitive with other growth probes. This method requires accurate modeling of completeness and contamination of cluster catalogs, projection effects on cluster selection and weak lensing measurements, and possible baryonic physics effects on the mass distribution within clusters.

Redshift-Space Distortions (RSD) and the Alcock-Paczynski (AP) Effect: Redshift-space distortions of galaxy clustering, induced by peculiar motions, probe structure growth by constraining the parameter combination $f(z)\sigma_8(z)$, where $f(z)$ is the growth rate defined by Eq. (28.3). Uncertainties in theoretical modeling of non-linear gravitational evolution and the non-linear bias between the galaxy and matter distributions currently limit application of the method to large scales (comoving separations $r \gtrsim 10\,h^{-1}$Mpc or wavenumbers $k \lesssim 0.2h\,{\rm Mpc}^{-1}$). A second source of anisotropy arises if one adopts the wrong cosmological metric to convert angles and redshifts into comoving separations, a phenomenon known as the Alcock-Paczynski effect [27]. Demanding isotropy of clustering at redshift z constrains the parameter combination $H(z)D_{\rm A}(z)$. The main challenge for the AP method is correcting for the anisotropy induced by peculiar velocity RSD.

Low Redshift Measurement of H_0: The value of H_0 sets the current value of the critical density $\rho_{\rm c} = 3H_0^2/8\pi G_{\rm N}$, and combination with CMB measurements provides a long lever arm for constraining the evolution of dark energy. The challenge in conventional H_0 measurements is establishing distances to galaxies that are "in the Hubble flow," *i.e.*, far enough away that their peculiar velocities are small compared to the expansion velocity $v = H_0 d$. This can be done by building a ladder of distance indicators tied to stellar parallax on its lowest rung, or by using gravitational-lens time delays or geometrical measurements of maser data to circumvent this ladder.

28.3.2 *Dark Energy Experiments*

Most observational applications of the above methods now take place in the context of large cosmological surveys, for which constraining dark energy and modified gravity theories is a central objective. Table 28.1 lists a selection of recent, ongoing, and planned dark-energy experiments, taken originally from the Snowmass 2013 Dark Energy Facilities review [28], which focused on projects in which the U.S. has either a leading role or significant participation. References and links to further information about these projects can be found in Ref. [28]. We have adjusted some of the dates in this Table relative to those in Ref. [28] and added the European-led KiloDegree Survey (KiDS). Dates in the Table correspond to the duration of survey observations, and the final cosmological results frequently require 1–3 years of analysis and modeling beyond the end of data taking. We are now at an exciting phase in which most of the "Stage III" experiments (in the parlance of Ref. [29]) have completed observations and in some cases final analysis, and the more powerful "Stage IV" experiments are underway or beginning operations in the near future.

Beginning our discussion with imaging surveys, the Dark Energy Survey (DES) observed 1/8 of the sky to a depth roughly 2 magnitudes deeper than the Sloan Digital Sky Survey (SDSS),

Table 28.1: A selection of major dark-energy experiments, based on Ref. [28]. Abbreviations in the "Data" column refer to optical (Opt) or near-infrared (NIR) imaging (I) or spectroscopy (S). For spectroscopic experiments, the "Spec-z" column lists the primary redshift range for galaxies (gals), quasars (QSOs), or the Lyman-α forest (LyαF). Abbreviations in the "Methods" column are weak lensing (WL), clusters (CL), supernovae (SN), baryon acoustic oscillations (BAO), and redshift-space distortions (RSD).

Project	Dates	Area/deg^2	Data	Spec-z Range	Methods
BOSS	2008–2014	10,000	Opt-S	0.3–0.7 (gals)	BAO/RSD
				2–3.5 (LyαF)	
KiDS	2011–2019	1350	Opt-I	——	WL/CL
DES	2013–2019	5000	Opt-I	——	WL/CL
					SN/BAO
eBOSS	2014–2018	7500	Opt-S	0.6–2.0 (gal/QSO)	BAO/RSD
				2–3.5 (LyαF)	
SuMIRE	2014–2029	1500	Opt-I		WL/CL
			Opt/NIR-S	0.8–2.4 (gals)	BAO/RSD
DESI	2021–2026	14,000	Opt-S	0–1.7 (gals)	BAO/RSD
				2–3.5 (LyαF)	
VRO/LSST	2025–2035	20,000	Opt-I	——	WL/CL
					SN/BAO
Euclid	2023–2029	15,000	Opt-I		WL/CL
			NIR-S	0.7–2.2 (gals)	BAO/RSD
Roman	2027–2032	2200	NIR-I		WL/CL/SN
			NIR-S	1.0–3.0 (gals)	BAO/RSD

enabling weak lensing measurements with much greater statistical precision, cluster measurements calibrated by weak lensing, and angular BAO measurements based on photometric redshifts. With repeated imaging of selected fields, DES identified thousands of Type Ia SNe, which together with spectroscopic follow-up data enabled significant improvements for supernova (SN) cosmology. Cosmological results from weak lensing and galaxy clustering analyses of the 3-year (Y3) DES data set are presented in Ref. [30]. The first cosmological results from the DES supernova survey are presented in Ref. [31], and DES supernovae are incorporated into the Pantheon+ compilation analyzed in Ref. [26]. KiDS carried out an optical imaging survey of about 1000 deg^2, with cosmology results from weak lensing and galaxy clustering reported in Refs. [32,33]. The Subaru Hyper-Suprime Camera (HSC) collaboration is surveying about 1500 deg^2 with greater depth and sharper image quality than DES; cosmology results from the 3-year HSC data set are presented in Refs. [34,35]. Beginning in the mid-2020s, the Legacy Survey of Space and Time (LSST) of the Vera Rubin Observatory (VRO) will scan the southern sky to SDSS-like depth every four nights. The co-added data from LSST's decade-long primary survey will provide deep multi-band imaging over a wide area, enabling weak lensing, cluster, and photometric BAO studies from billions of galaxies. Additionally, LSST time-domain monitoring will identify and measure light curves for thousands of Type Ia SNe per year.

Turning to spectroscopic surveys, the Baryon Oscillation Spectroscopic Survey (BOSS) and its successor eBOSS used fiber-fed optical spectrographs to map the redshift-space distributions of

millions of galaxies and quasars. These 3-dimensional maps enable BAO and RSD measurements, and Lyman-α forest spectra of high-redshift quasars extend these measurements to redshifts $z > 2$. As discussed below, the eBOSS Collaboration has now published BAO and RSD analyses from the final data sets of the BOSS and eBOSS programs. The Dark Energy Spectroscopic Instument (DESI) follows a strategy similar to BOSS/eBOSS but on a much grander scale, using a larger telescope (4-m versus 2.5-m) and a much higher fiber multiplex (5000 versus 1000) to survey an order-of-magnitude more galaxies. DESI began full operations in May 2021, and in its first two years it has measured well over 20 million redshifts; at least 40 million redshifts are expected by the survey end. A new Prime Focus Spectrograph (PFS) for the Subaru telescope will enable the spectroscopic component of SuMIRE, starting in 2024, with the large telescope aperture and wavelength sensitivity that extends to the near-infrared (NIR) allowing it to probe a higher redshift galaxy population than DESI, over a smaller area of sky.

Compared to ground-based observations, space observations afford higher angular resolution and a far lower NIR sky background. The *Euclid* mission and the *Nancy Grace Roman Space Telescope* (formerly *WFIRST*) will exploit these advantages, conducting large area imaging surveys for weak lensing and cluster studies and slitless spectroscopic surveys of emission-line galaxies for BAO and RSD studies. *Roman* will also incorporate an imaging and spectrophotometric supernova (SN) survey, extending to redshift $z \simeq 1.7$. One can roughly characterize the difference between the *Euclid* and *Roman* dark-energy experiments as "wide versus deep," with currently planned survey areas of 15,000 deg^2 and 2200 deg^2, respectively. For weak lensing shape measurements, *Euclid* uses a single wide optical filter, while *Roman* will use three NIR filters. The *Euclid* galaxy redshift survey will cover a large volume at relatively low space density, while the *Roman* survey will provide denser sampling of structure in a smaller volume. *Euclid* was launched successfully in July 2023 and has released first light images; it will begin its 6.5-year main mission survey in late 2023. *Roman* is scheduled for launch in late 2026 or early 2027, and details of its cosmology surveys will likely evolve before operations begin. There are numerous synergies among the LSST, *Euclid*, and *Roman* dark energy programs, as discussed in Ref. [36].

28.4 Current Constraints on Expansion, Growth, and Dark Energy

The last decade has seen dramatic progress in measurements of the cosmic expansion history and structure growth, leading to much tighter constraints on the parameters of dark energy models. CMB data from the *WMAP* and *Planck* satellites and from higher resolution ground-based experiments have provided an exquisitely detailed picture of structure at the recombination epoch and CMB-based measures of low-redshift structure through lensing and SZ cluster counts. Cosmological supernova samples have increased in size from tens to thousands, with continuous coverage from $z = 0$ to $z \simeq 1.4$, alongside major improvements in data quality, analysis methods, and detailed understanding of local populations. BAO measurements have advanced from the first detections to 1–2% precision at multiple redshifts, with increasingly sophisticated methods for testing systematics, fitting models, and evaluating statistical errors. Advances in X-ray, SZ, and weak-lensing observations of large samples of galaxy clusters allow a multi-faceted approach to mass calibration, improving statistical precision but also revealing sources of astrophysical uncertainty. Cluster constraints have been joined, and for the present superseded, by precise matter-clustering constraints from cosmic-shear weak lensing and galaxy-galaxy lensing, and by redshift-space distortion measurements that probe different aspects of structure growth at (presently) lower precision. The precision of low-redshift H_0 measurements has sharpened from the roughly 10% error of the *HST* Key Project [37] to claimed precision as high as 1–2% in recent analyses.

As an illustration of current measurements of the cosmic expansion history, Fig. 28.1 compares distance-redshift measurements from SN and BAO data to the predictions for a flat Universe with

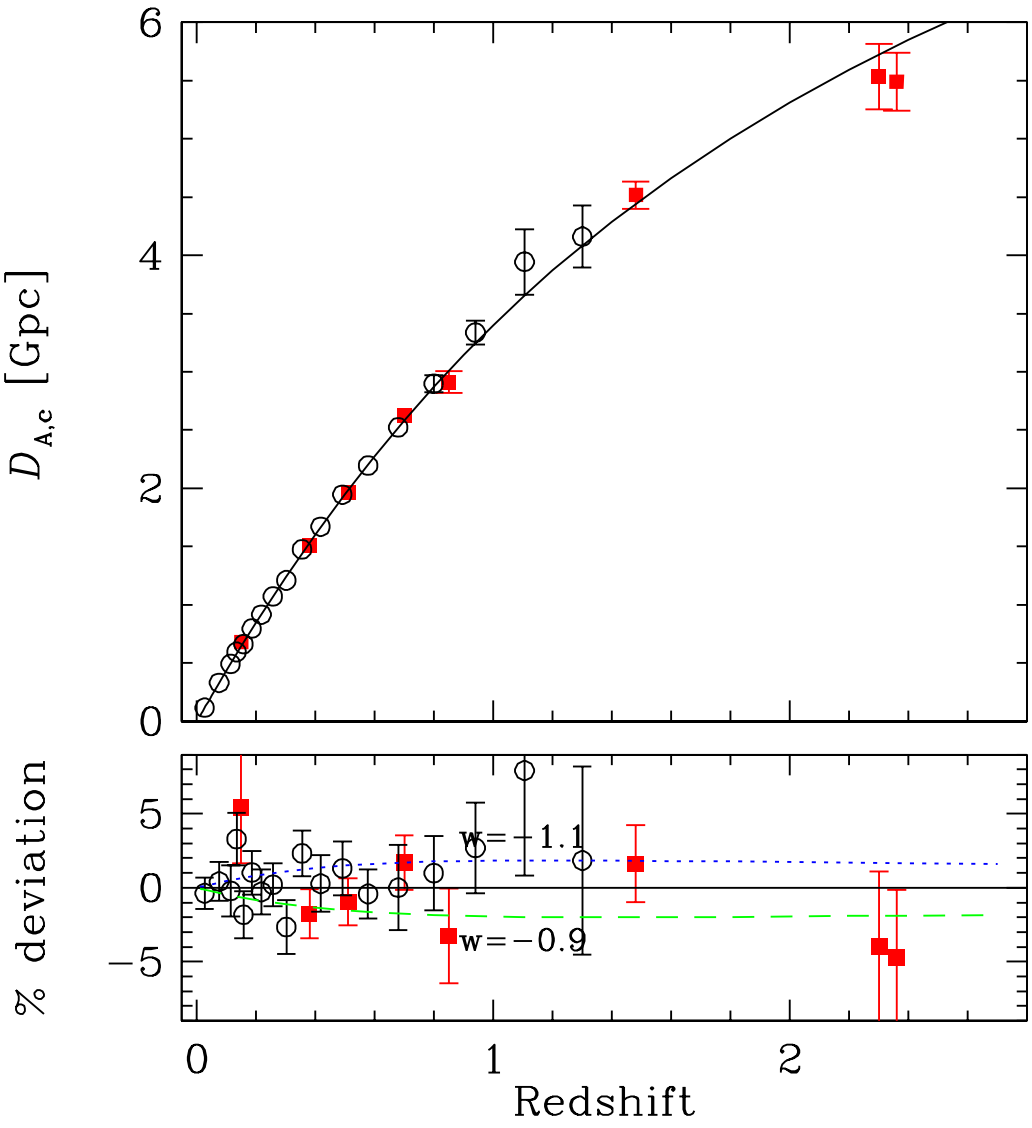

Figure 28.1: Distance-redshift relation measured from Type Ia SNe and BAO compared to the predictions (black curve) of a flat ΛCDM model with $\Omega_m = 0.315$ and $h = 0.674$, the best-fit parameters inferred from *Planck* CMB data [38]. Circles show binned luminosity distances from the JLA SN sample [39], multiplied by $(1+z)^{-1}$ to convert to comoving angular diameter distance. Red squares show BAO distance measurements from the SDSS-II, BOSS, and eBOSS surveys as compiled in Ref. [40]. The lower panel plots residuals from the ΛCDM prediction, with dashed and dotted curves that show the effect of changing w by ± 0.1 while all other parameters are held fixed. Note that the SN data points can be shifted up or down by a constant factor to account for freedom in the peak luminosity, while the BAO points are calibrated to 0.2% precision by the sound horizon scale computed from *Planck* data. The errors on the BAO data points are approximately independent, but not entirely so. In the upper panel, error bars are plotted only at $z > 0.7$ to avoid visual confusion. The two Lyman-α forest data points are slightly offset from their effective redshift of $z = 2.33$ for clarity.

a cosmological constant. SN cosmology relies on compilation analyses that try to bring data from different surveys probing distinct redshift ranges to a common scale. Here we use the "joint light curve analysis" (JLA) sample of Ref. [39], who carried out a careful intercalibration of the 3-year Supernova Legacy Survey (SNLS3, [41]) and the full SDSS-II Supernova Survey [3] data in combination with several local supernova samples and high-redshift supernovae from *HST*. For illustration purposes, we have binned the JLA data in redshift and plotted the diagonal elements of the covariance matrix as error bars, and we have converted the SN luminosity distances to an equivalent comoving angular diameter distance. Because the peak luminosity of a fiducial SN Ia is an unknown free parameter, the SN distance measurements could all be shifted up and down by a constant multiplicative factor; cosmological information resides in the relative distances as a function of redshift. The normalization used here corresponds to a Hubble parameter $h = 0.674$.

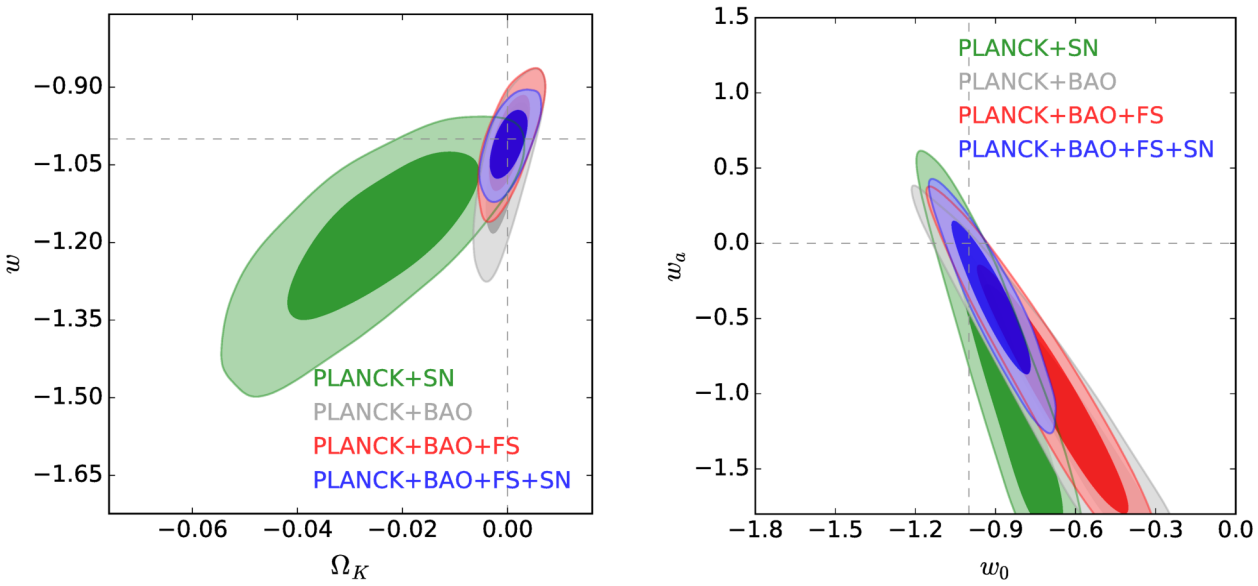

Figure 28.2: Constraints on dark energy model parameters from combinations of CMB, BAO, galaxy clustering, and supernova (SN) data, taken from Ref. [42]. The left panel shows 68% and 95% confidence contours in the `owCDM` model, with constant equation-of-state parameter w and non-zero space curvature $\Omega_K \equiv 1 - \Omega_{\rm tot}$. Green and gray contours show the combination of *Planck* CMB data with SN or BAO data, respectively. Red contours combine CMB, BAO, and the full shape (FS) of redshift-space galaxy clustering. Blue contours add SN data to this combination. The right panel shows confidence contours for the same data combinations in the $\mathtt{w_0w_aCDM}$ model, which assumes a flat Universe and an evolving equation of state with $w(a) = w_0 + w_{\rm a}(1 - a)$.

For the BAO data points in Fig. 28.1 we have used the compilation in Table 3 (the "BAO-only" row) from the summary cosmology paper by the eBOSS collaboration [40], where one can find references for the original data sources. The individual BAO measurements come (in order of increasing redshift) from the SDSS-II main galaxy sample and from luminous red galaxies, emission line galaxies, and quasars mapped by BOSS and eBOSS. The two highest redshift points, both with an effective $z \approx 2.3$, come from the auto-correlation of the Lyman-α forest in high-redshift ($z > 2$) quasars from BOSS and eBOSS and from the cross-correlation of the Lyman-α forest with the quasars themselves. The BAO measurements are converted to absolute distances using the sound horizon scale $r_{\rm s} = 147.09$ Mpc from *Planck* 2018 CMB data, whose 0.18% uncertainty is small compared to the current BAO measurement errors. For the $z = 0.15$ and $z = 1.5$ data points

we have converted values of D_V to $D_{A,c}$, while for other redshifts we use the $D_{A,c}$ determinations measured directly by the transverse BAO scale. The galaxy and Lyman-α forest analyses also measure $H(z)$ at the same redshifts, providing further leverage on expansion history that is not captured in Fig. 28.1.

The plotted cosmological model has $\Omega_m = 0.315$ and $h = 0.674$, the best-fit values from *Planck* (TT+TE+EE+lowE+lensing) assuming $w = -1$ and $\Omega_{tot} = 1$ [38]. The SN, BAO, and CMB data sets, probing a wide range of redshifts with radically different techniques, are for the most part mutually consistent with the predictions of a flat ΛCDM cosmology. This consistency has held steady or improved as the measurements themselves have improved over the past decade. Dotted and dashed curves in the lower panel of Fig. 28.1 show the effect of changing w by ± 0.1 with all other parameters held fixed, which leads to significantly worse agreement with the data. However, such a single-parameter comparison does not capture the impact of parameter degeneracies or the ability of complementary data sets to break them, and if one instead forced a match to CMB data by changing h and Ω_m when changing w then the predicted BAO distances would diverge at $z = 0$ rather than converging there. The recent Pantheon+ compilation [43] comprises more than 1500 spectroscopically confirmed Type Ia supernovae from 18 different samples, including those in the JLA. With higher statistical precision and reduced systematic uncertainties, a joint fit of Pantheon+ with CMB and BAO data remains fully compatible with a flat ΛCDM model [26]. Other good representations of recent observational constraints on the cosmic expansion history include Fig. 4 of Ref. [26] for SNIa and Fig. 2 of Ref. [40] for BAO.

Fig. 28.2, taken from Ref. [42], presents constraints on models that allow a free but constant value of w with non-zero space curvature (`owCDM`, left panel) or the evolving equation of state of Eq. (28.4) in a flat Universe ($\mathtt{w_0w_aCDM}$, right panel). Green contours show constraints from the combination of *Planck* 2015 CMB data and the JLA supernova sample. Gray contours show the combination of *Planck* with BAO measurements from BOSS, 6dFGS [44], and SDSS-II [45]. Red contours adopt a more aggressive analysis of the BOSS galaxy data that uses the full shape (FS) of the redshift-space power spectrum and correlation function, modeled via perturbation theory, in addition to the measurement of the BAO scale itself. The full shape analysis improves the constraining power of the data, primarily because measurement of the Alcock-Paczynski effect on sub-BAO scales helps to break the degeneracy between $D_{A,c}(z)$ and $H(z)$. Blue contours show constraints from the full combination of CMB, BAO+FS, and SN data. Supernovae provide fine-grained relative distance measurements with good bin-by-bin precision at $z < 0.7$ (see Fig. 28.1), which is complementary to BAO for constraining redshift evolution of w. In both classes of model, the flat ΛCDM parameters ($w = w_0 = -1$, $\Omega_K = w_a = 0$) lie within the 68% confidence contour. Many recent papers feature constraint diagrams analogous to Fig. 28.2, and the constraints within this parameter space have tightened moderately with new data while remaining consistent with flat ΛCDM.

The precision on dark energy parameters depends, of course, on both the data being considered and the flexibility of the model being assumed. For `wCDM`, Ref. [40] find $w = -1.026 \pm 0.033$ using *Planck* CMB data, BAO measurements from SDSS-II and BOSS/eBOSS, and SN measurements from the Pantheon compilation. With the addition of eBOSS RSD data and DES weak lensing and galaxy clustering measurements, they constrain a more flexible model ($\mathtt{ow_0w_aCDM}$) that allows non-zero curvature and an evolving equation-of-state (Eq. 28.4), finding

$$w_p = -1.020 \pm 0.032 \tag{28.5}$$

at a pivot redshift $z_p = 0.29$, a tight constraint on curvature,

$$1 - \Omega_{tot} = -0.0023 \pm 0.0022 \ , \tag{28.6}$$

but only a loose constraint on the evolution parameter,

$$w_{\rm a} = -0.48^{+0.36}_{-0.30}. \tag{28.7}$$

Obtaining a tight constraint on $w_{\rm p}$ in such a flexible cosmological model requires measurements that have complementary sensitivity to its multiple free parameters, and the precision of Eq. (28.5) is a testament to the remarkable improvements in cosmological measurements over the past decade. BAO and FS measurements from DESI will likely supersede those from BOSS/eBOSS in the near future, enabling substantially sharper parameter constraints.

A flat ΛCDM model fit to *Planck* CMB data alone predicts $H_0 = (67.4 \pm 0.5)$ km s^{-1} Mpc^{-1} (see Chapter 29 of this *Review*). This prediction and its error bar are sensitive to the assumptions of constant dark energy and a flat Universe. However, by adding BAO and supernova data one can construct an "inverse distance ladder" to measure H_0 precisely, even with a general dark energy model and free curvature [46]. Ref. [40] applies this approach to obtain $H_0 = (68.2 \pm 0.8)$ km s^{-1} Mpc^{-1}. As discussed in Sec. 25.3.1 of this *Review*, some recent measurements from low-redshift data yield higher values of H_0. For example, Ref. [47] uses a distance ladder based on Cepheid calibration of Type Ia supernova luminosities to find $H_0 = (73.0 \pm 1.0)$ km s^{-1} Mpc^{-1}, in strong tension with cosmologically inferred values. However, calibrations based on tip-of-the-red-giant-branch (TRGB) distances give lower H_0, consistent with the cosmological values [48].

The tension in H_0 could reflect some combination of statistical flukes and systematic errors in one or more of the data sets employed in these analyses. However, if the resolution lies in new physics rather than measurement errors, then this is probably physics that operates in the *pre-recombination* Universe, rescaling the BAO standard ruler in a way that shifts the ΛCDM and inverse-distance-ladder values upward. Models with extra relativistic degrees of freedom or dark energy that is dynamically significant in the early Universe can achieve this effect by increasing the early expansion rate, but they are tightly constrained by the damping tail of CMB anisotropies and by the shape of the galaxy power spectrum. These constraints will sharpen significantly with the next generation of CMB experiments, which will improve measurements of polarization anisotropies in the damping tail. A finely tuned model in which early dark energy decays rapidly after recombination can mitigate the tension between CMB data and local H_0 measurements [49], though it still prefers H_0 values below those of Ref. [47]. Numerous theory papers have examined possible physical solutions to the H_0 tension, all of which involve significant modifications to the ΛCDM scenario.

The amplitude of CMB anisotropies is proportional to the amplitude of density fluctuations present at recombination, and by assuming GR and a specified dark energy model one can extrapolate the growth of structure forward to the present day to predict σ_8. Probes of low-redshift structure yield constraints in the $(\sigma_8, \Omega_{\rm m})$ plane, which can be summarized in terms of the parameter combination $S_8 \equiv \sigma_8(\Omega_{\rm m}/0.3)^{0.5}$. As discussed in earlier editions of this *Review*, many weak-lensing and cluster studies to date yield S_8 values lower than those predicted for *Planck*-normalized ΛCDM.

Fig. 28.3, taken from Ref. [50], illustrates the current state-of-play on S_8. (Similar figures with different selections of data can be found in many recent papers and in the previous edition of this *Review*.) The topmost point represents the predicted value and 1σ uncertainty, $S_8 = 0.830 \pm 0.014$, based on a flat ΛCDM model normalized to *Planck* CMB anisotropies. The next two points illustrate a different treatment of the *Planck* data or an alternative CMB data combination. The next four points, in red, illustrate values of S_8 measured from weak lensing of the CMB, again assuming flat ΛCDM. Although the background being lensed is the CMB, this is still a measurement of low-redshift clustering; for multipoles $\ell > 100$ roughly half of the expected signal comes from structure at $z < 2$ and nearly all from $z < 10$ [51].

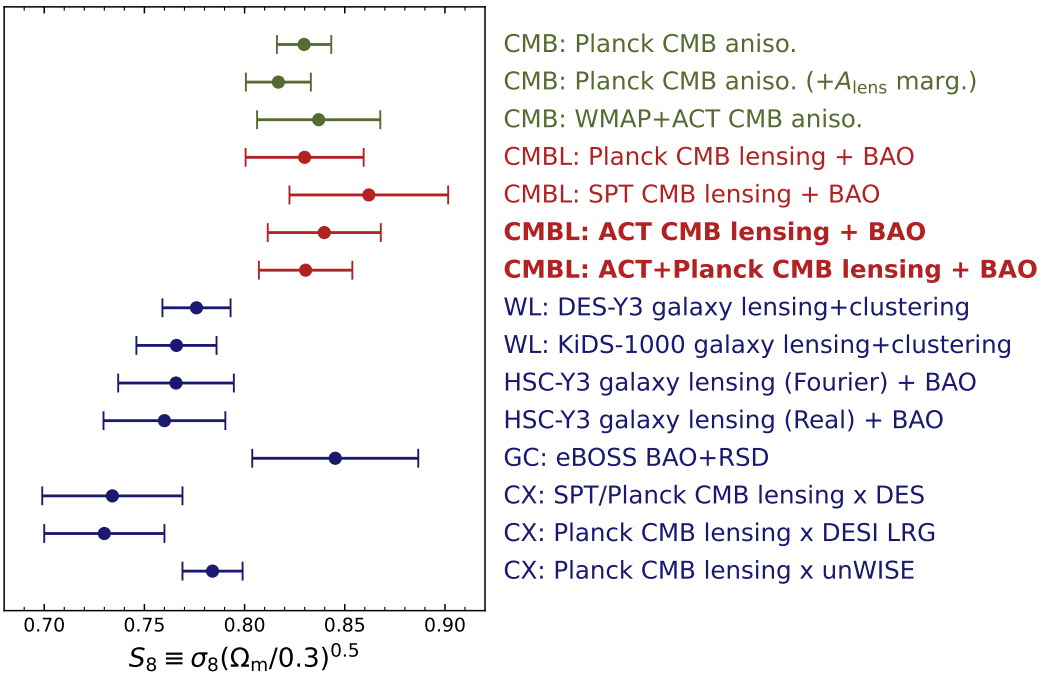

Figure 28.3: Predicted values of $S_8 \equiv \sigma_8(\Omega_m/0.3)^{0.5}$ from a CMB-normalized ΛCDM model (green points), compared to observational estimates from CMB lensing (red points), from optical weak lensing surveys (first four blue points), from galaxy clustering RSD (blue GC point), and from cross-correlation of galaxies with CMB lensing maps (blue CX points). The predictions (green) are extrapolated forward from primary CMB anisotropy measurements that measure structure at $z \approx 1100$. CMB lensing (red) is most sensitive to structure at $z \approx 1-2$, while the galaxy-based data (blue) probe structure at $z \approx 0.2$–0.8. Taken from Ref. [50].

The remaining points, in blue, represent galaxy-based measurements that probe structure at $z \approx 0.2$–0.8, lower than the peak of the CMB-lensing kernel. The first four come from analyses of the DES, KiDS, and HSC weak lensing surveys, using cosmic shear and galaxy-galaxy lensing combined with galaxy clustering. The three points labeled CX come from cross-correlation of galaxies with CMB lensing maps, which measures the galaxy-matter cross-correlation without using optical weak lensing data. The point labeled GC (fourth from bottom) is inferred from RSD analysis of eBOSS galaxies. Details and references can be found in Sec. 3.4 of Ref. [50].

It is evident from Fig. 28.3 that CMB lensing measurements of S_8 (red points) are in good agreement with predictions based on primary CMB anisotropy (green points), but S_8 values measured from weak lensing at lower redshifts are consistently lower than this prediction (blue points, excluding the GC point derived from RSD). The discrepancy with any individual measurement is only 1–2σ, but the significance is higher if one treats the points derived from separate surveys as statistically independent. For instance, after averaging the two HSC measurements, an unweighted mean of the six low redshift lensing measurements in Fig. 28.3 yields $S_8 = 0.759 \pm 0.009$, where the 1σ error is simply the dispersion of the measurements divided by $\sqrt{N-1} = \sqrt{5}$. With this estimate, the $+3\sigma$ bound $S_8 = 0.786$ lies just below the -3σ bound of the *Planck* prediction, $S_8 = 0.788$. However, several or all of these measurements could be affected by a common systematic error, such as the modeling of galaxy intrinsic alignments or the modeling of structure on non-linear scales. Furthermore, the RSD measurement, which probes similar redshifts with a physically distinct ob-

servable, gives a much higher S_8 value, though with an uncertainty large enough to accommodate both the CMB-based prediction and the low-z weak lensing measurement.

The tension between the ΛCDM prediction of S_8 and low redshift weak lensing measurements has persisted through several cycles of this *Review*, without getting obviously stronger or obviously weaker. The sharpest conflicts arise in analyses that extend to non-linear scales and thus have the highest statistical precision, but these analyses are also the most susceptible to modeling uncertainties such as the impact of baryonic dissipation and feedback on the mass distribution. If the tension suggested by Fig. 28.3 represents a true deviation between the clustering growth extrapolated forward from the early Universe and the clustering of matter at late times, then it is difficult to explain by changing the dark energy equation of state because the expansion history is already well constrained by BAO and SN data. Instead, such a deviation might point towards modified gravity, decaying dark matter, or coupling between dark matter and dark energy.

Progress in understanding this tension should come from several directions. Unified analyses of multiple weak lensing data sets are now testing consistency and highlighting the influence of analysis choices on cosmological results [52, 53]. Final data from DES and HSC will have better statistical power, which improves the internal calibration of systematic nuisance parameters and affords greater precision at the larger scales that are easier to model. Improved CMB lensing maps will allow better cross-correlation measurements (the CX points in Fig. 28.3), which avoid some of the main systematics affecting optical weak lensing. DESI data will soon allow the first RSD-based measurements of structure growth at the 1–2% level, which will show whether the low matter clustering amplitude suggested by weak lensing data is also apparent in galaxy peculiar velocities. In modified gravity models these two methods of constraining structure can yield inconsistent results because they respond to different combinations of metric components, but either consistency or inconsistency would provide valuable guidance. Finally, if there is truly a 5–10% discrepancy between CMB-normalized ΛCDM predictions and low-redshift clustering, it should be measured at high statistical significance in *Euclid* weak lensing data and, subsequently, in LSST and *Roman* data.

28.5 Summary and Outlook

Figure 28.2 focuses on model parameter constraints, but to describe the observational situation it is more useful to characterize the precision, redshift range, and systematic uncertainties of the basic expansion and growth measurements. At present, supernova surveys constrain distance ratios at the 1–2% level in redshift bins of width $\Delta z = 0.1$ out to $z \approx 0.8$, with larger but still interesting error bars out to $z \simeq 1.3$. Estimated systematic uncertainties are comparable to statistical uncertainties and include effects of photometric calibration, dust reddening, host-galaxy correlations, and possible evolution of the SN population. BAO surveys have measured the angular diameter distance $D_{\rm A,c}(z)$ and the expansion rate $H(z)$ over the range $0 < z < 2.5$, calibrated to absolute units using the CMB-based value of the sound horizon $r_{\rm s}$. For $D_{\rm A,c}(z)$, the final analyses of BOSS/eBOSS achieve precision of 1.6–1.8% in three overlapping redshift bins from luminous galaxies at $z = 0.2-1.0$, 2.6% from quasars at $z \approx 1.5$, and 2.9% from the Lyman-α forest at $z \approx 2.3$. For $H(z)$, the precision at the same redshifts is 2.6–3.0%, 4.1%, and 2.1%, respectively. SDSS, DES, KiDS, and HSC have used combinations of weak lensing and galaxy clustering to measure the parameter combination $S_8 = \sigma_8(\Omega_{\rm m}/0.3)^{0.5}$ with estimated precision of 2–4%, and the cross-correlation of galaxy distributions with CMB lensing maps achieves comparable precision. These estimates account for identified systematic uncertainties, but the measurements and modeling are challenging, and it is possible that the systematics are underestimated. Our simple average of these measurements, treating them as independent and using their dispersion as an empirical estimate of uncertainty, yields an error on the mean of 1.1%. The statistical power of these weak lensing surveys is concentrated at

$z \approx 0.2$–0.8, and they provide useful constraints at lower precision on redshift evolution over this range and on individual values of $\Omega_{\rm m}$ and σ_8. RSD measurements constrain the similar parameter combination $f(z)\sigma_8(z)$, but they do not yet have precision competitive with that of weak lensing measurements. Distance-ladder estimates of H_0 now span a small range, using overlapping data but distinct treatments of key steps. Individual studies quote uncertainties as small as 1–2%, with similar statistical and systematic contributions.

Planck data and higher resolution ground-based experiments now measure CMB anisotropies with exquisite precision; for example, CMB measurements now constrain the physical size of the BAO sound horizon to 0.2% and the angular scale of the sound horizon to 0.01%. A flat ΛCDM model with standard radiation and neutrino content can fit the CMB data and the BAO and SN distance measurements to within their estimated uncertainties. The value of H_0 implied by this model disagrees with recent Cepheid+SNIa distance-ladder measurements of H_0 at a $\sim 5\sigma$ level. This disagreement persists in models that allow non-zero curvature and low redshift evolution of $w(z)$, provided one assumes standard pre-recombination physics to compute the sound horizon $r_{\rm s}$. The discrepancy could reflect underestimated systematic uncertainties in the Cepheid-based H_0 estimate, or it could be a sign of new physics in the early Universe that rescales $r_{\rm s}$. Improved parallax data from *HST* and *Gaia*, discovery of new SNIa in nearby galaxies, and observing programs on the *James Webb Space Telescope* (*JWST*) are all allowing improvements and systematics checks in the Cepheid distance ladder. It will be equally important to bring the TRGB calibration method to a comparable level of precision and systematics control, and to understand any differences between the Cepheid and TRGB distance scales. Polarization measurements of the CMB damping tail from ground-based experiments will provide increasingly strong constraints on resolutions of the H_0-tension that invoke novel pre-recombination physics.

Extrapolating forward from the CMB anisotropies measured by *Planck* predicts a low redshift value of S_8 that is higher than recent estimates from weak gravitational lensing and galaxy clustering. Comparing the *Planck* central value to the simple average of recent experiments discussed in Sec.28.4 implies a difference of 9.3%: $S_8 = 0.830 \pm 0.014$ versus $S_8 = 0.759 \pm 0.009$. This disagreement could reflect a common systematic that biases several of the weak lensing analyses in the same direction, and it would be weakened if the *Planck* S_8 value were high because of an unlucky statistical fluctuation or a residual systematic. If real, this discrepancy could point towards modified gravity, decaying dark matter, or coupling between dark matter and dark energy.

There are numerous directions for progress over the next several years. Analyses of the final weak lensing data sets from KiDS, HSC, and DES will yield tighter statistical constraints and more complete understanding of systematic uncertainties. Cross-correlation of galaxy maps with higher signal-to-noise CMB lensing maps will provide independent clustering measurements that avoid many of the systematics of optical weak lensing. Collectively these efforts could achieve an unambiguous determination of the amplitude of low redshift matter clustering at the 1–2% level.

The DESI redshift survey already exceeds the size of the SDSS and BOSS/eBOSS surveys, with a factor of ~ 10 increase expected by the end of the 5-year program. DESI will enable the first high precision BAO measurements of expansion history at $z \approx 0.7$–1.4, as well as improved BAO measurements at $z < 0.7$ from denser galaxy samples and at $z > 2$ from much larger Lyman-α forest samples. DESI will also enable the first percent-level measurements of structure growth through RSD. The BAO measurements will complement increasingly precise measurements of the relative distance scale at $z < 1$ from supernova compilations that include the final data from DES. Large galaxy samples will also enable more powerful applications of the Alcock-Paczynski effect and parameter measurements based on voids or higher order clustering statistics.

Euclid, LSST, and *Roman* provide another major leap in observational capabilities. LSST will be the ultimate ground-based optical weak-lensing experiment, measuring several billion galaxy

shapes over 20,000 deg^2 of the southern hemisphere sky, and it will detect and monitor many thousands of SNe per year. *Euclid* and *Roman* also have weak lensing as a primary science goal, taking advantage of the high angular resolution and extremely stable image quality achievable from space. Both missions plan large spectroscopic galaxy surveys, which will provide better sampling at high redshifts than DESI or Subaru PFS because of the lower infrared sky background above the atmosphere. *Roman* is also designed to carry out what should be the ultimate supernova cosmology experiment, with deep, high resolution, near-IR observations and the stable calibration achievable with a space platform. The 2020s will also see dramatic advances in CMB lensing from the Simons Observatory and, potentially, CMB-S4 and/or a space-based probe; cross-correlation with galaxy surveys allows precise tomographic studies of clustering as a function of redshift. While the measurement goals of these next generation facilities overlap, the history of precision cosmology demonstrates the crucial importance of pursuing these measurements with multiple experiments that have distinct challenges and complementary strengths, and with analysis teams that develop ideas independently. The ensemble of experiments will produce cosmological constraints that are much tighter and much more robust to systematic uncertainties than any one of them could achieve individually.

If the anomalies suggested in Fig. 28.3 are real, then these experiments will map out their redshift, scale, and environment dependence in great detail, providing detailed empirical constraints on dynamical dark energy or modified gravity models. If these tensions dissipate with improved measurements, then the experiments of the 2020s will achieve much more stringent tests of the ΛCDM paradigm, with the potential to reveal deviations that are still within the statistical uncertainties of current data. The critical clue to the origin of cosmic acceleration could also come from a surprising direction, such as laboratory, solar-system, or gravitational-wave tests that challenge GR, time variation of fundamental "constants," or anomalous behavior of gravity in some astronomical environments. Experimental advances along these multiple axes could confirm today's relatively simple, but frustratingly incomplete, "standard model" of cosmology, or they could force yet another radical revision in our understanding of energy, or gravity, or the spacetime structure of the Universe.

References

[1] A. Einstein, Sitzungsber. Preuss. Akad. Wiss. Berlin (Math. Phys.), 142 (1917).

[2] Ya. B. Zel'dovich, A. Krasinski and Ya. B. Zeldovich, Sov. Phys. Usp. **11**, 381 (1968), [Gen. Rel. Grav.40,1557(2008); Usp. Fiz. Nauk95,209(1968)].

[3] A. Friedman, Z. Phys. **10**, 377 (1922), [Gen. Rel. Grav.31,1991(1999)].

[4] G. Lemaître, Annales de la Societe Scietifique de Bruxelles **47**, 49 (1927).

[5] E. Hubble, Proc. Nat. Acad. Sci. **15**, 168 (1929).

[6] A. Einstein and W. de Sitter, Proc. Nat. Acad. Sci. **18**, 213 (1932).

[7] For background and definitions, see Big-Bang Cosmology – Sec. 22 of this *Review*.

[8] A. G. Riess *et al.* (Supernova Search Team), Astron. J. **116**, 1009 (1998), [arXiv:astro-ph/9805201].

[9] S. Perlmutter *et al.* (Supernova Cosmology Project), Astrophys. J. **517**, 565 (1999), [arXiv:astro-ph/9812133].

[10] P. de Bernardis *et al.* (Boomerang), Nature **404**, 955 (2000), [arXiv:astro-ph/0004404].

[11] S. Hanany *et al.*, Astrophys. J. **545**, L5 (2000), [arXiv:astro-ph/0005123].

[12] D. H. Weinberg *et al.*, Phys. Rept. **530**, 87 (2013), [arXiv:1201.2434].

[13] C. Wetterich, Nucl. Phys. **B302**, 668 (1988), [arXiv:1711.03844].

[14] A. Joyce *et al.*, Phys. Rept. **568**, 1 (2015), [arXiv:1407.0059].

[15] S. M. Carroll *et al.*, Phys. Rev. **D70**, 043528 (2004), [arXiv:astro-ph/0306438].

[16] G. R. Dvali, G. Gabadadze and M. Porrati, Phys. Lett. **B485**, 208 (2000), [hep-th/0005016].

[17] C.M. Will, Living Reviews in Relativity, **9**, 3 (2006). See also the chapter on Experimental Tests of Gravitational Theory — in this *Review*.

[18] J. Wang, L. Hui and J. Khoury, Phys. Rev. Lett. **109**, 241301 (2012), [arXiv:1208.4612].

[19] M. Fairbairn and A. Goobar, Phys. Lett. **B642**, 432 (2006), [arXiv:astro-ph/0511029]; Y.-S. Song, I. Sawicki and W. Hu, Phys. Rev. **D75**, 064003 (2007), [arXiv:astro-ph/0606286]; C. Blake *et al.*, Mon. Not. Roy. Astron. Soc. **415**, 2876 (2011), [arXiv:1104.2948].

[20] T. Baker *et al.*, Phys. Rev. Lett. **119**, 25, 251301 (2017), [arXiv:1710.06394].

[21] E. V. Linder, Phys. Rev. **D72**, 043529 (2005), [arXiv:astro-ph/0507263].

[22] This is essentially the FoM proposed in the Dark Energy Task Force (DETF) report, A. Albrecht *et al.*, `astro-ph/0609591,`though they based their FoM on the area of the 95% confidence contour in the $w_0 - w_a$ plane.

[23] T. Baker *et al.*, Rev. Mod. Phys. **93**, 1, 015003 (2021), [arXiv:1908.03430].

[24] For high accuracy, the impact of acoustic oscillations must be computed with a full Boltzmann code, but the simple integral for $r_{\rm s}$ captures the essential physics and the scaling with cosmological parameters.

[25] R. A. Sunyaev and Ya. B. Zeldovich, Astrophys. Space Sci. **7**, 3 (1970).

[26] D. Brout *et al.*, Astrophys. J. **938**, 2, 110 (2022), [arXiv:2202.04077].

[27] C. Alcock and B. Paczynski, Nature **281**, 358 (1979).

[28] D. Weinberg *et al.* (2013), [arXiv:1309.5380].

[29] A. Albrecht *et al.* (2006), [arXiv:astro-ph/0609591].

[30] T. M. C. Abbott *et al.* (DES) (2021), [arXiv:2105.13549].

[31] T. M. C. Abbott *et al.* (DES), Astrophys. J. **872**, 2, L30 (2019), [arXiv:1811.02374].

[32] M. Asgari *et al.* (KiDS), Astron. Astrophys. **645**, A104 (2021), [arXiv:2007.15633].

[33] C. Heymans *et al.*, Astron. Astrophys. **646**, A140 (2021), [arXiv:2007.15632].

[34] R. Dalal *et al.* (2023), [arXiv:2304.00701].

[35] X. Li *et al.* (2023), [arXiv:2304.00702].

[36] B. Jain *et al.* (2015), [arXiv:1501.07897].

[37] W. L. Freedman *et al.* (HST), Astrophys. J. **553**, 47 (2001), [arXiv:astro-ph/0012376].

[38] N. Aghanim *et al.* (Planck) (2018), [arXiv:1807.06209].

[39] M. Betoule *et al.*, Astron. & Astrophys. **568**, 22 (2014).

[40] S. Alam *et al.* (eBOSS), Phys. Rev. D **103**, 8, 083533 (2021), [arXiv:2007.08991].

[41] M. Sullivan *et al.* (SNLS), Astrophys. J. **737**, 102 (2011), [arXiv:1104.1444].

[42] S. Alam *et al.* (BOSS), Mon. Not. Roy. Astron. Soc. **470**, 3, 2617 (2017), [arXiv:1607.03155].

[43] D. Scolnic *et al.*, Astrophys. J. **938**, 2, 113 (2022), [arXiv:2112.03863].

[44] F. Beutler *et al.*, Mon. Not. Roy. Astron. Soc. **416**, 3017 (2011), [arXiv:1106.3366].

[45] A. J. Ross *et al.*, Mon. Not. Roy. Astron. Soc. **449**, 1, 835 (2015), [arXiv:1409.3242].

[46] E. Aubourg *et al.*, Phys. Rev. **D92**, 12, 123516 (2015), [arXiv:1411.1074].

[47] A. G. Riess *et al.*, Astrophys. J. Lett. **934**, 1, L7 (2022), [arXiv:2112.04510].
[48] S. A. Uddin *et al.* (2023), [arXiv:2308.01875].
[49] V. Poulin *et al.*, Phys. Rev. Lett. **122**, 22, 221301 (2019), [arXiv:1811.04083].
[50] M. S. Madhavacheril *et al.* (ACT) (2023), [arXiv:2304.05203].
[51] A. Lewis and A. Challinor, Phys. Rept. **429**, 1 (2006), [arXiv:astro-ph/0601594].
[52] A. Amon *et al.*, Mon. Not. Roy. Astron. Soc. **518**, 1, 477 (2023), [arXiv:2202.07440].
[53] T. M. C. Abbott *et al.* (Kilo-Degree Survey, DES) (2023), [arXiv:2305.17173].